

Evaporative cooling of the dipolar radical OH

Benjamin K. Stuhl¹, Matthew T. Hummon¹, Mark Yeo¹, Goulven Quémener¹, John L. Bohn¹, & Jun Ye¹

¹*JILA, National Institute of Standards and Technology and University of Colorado, and Department of Physics, University of Colorado, Boulder, CO 80309, USA.*

Atomic physics was revolutionized by the development of forced evaporative cooling: it led directly to the observation of Bose-Einstein condensation^{1,2}, quantum-degenerate Fermi gases³, and ultracold optical lattice simulations of condensed matter phenomena⁴. More recently, great progress has been made in the production of cold molecular gases⁵, whose permanent electric dipole moment is expected to generate rich, novel, and controllable phases^{6–8}, dynamics^{9–11}, and chemistry^{12–14} in these ultracold systems. However, while many strides have been made¹⁵ in both direct cooling and cold-association techniques, evaporative cooling has not yet been achieved due to unfavorable elastic-to-inelastic ratios¹³ and impractically slow thermalization rates in the available trapped species. We now report the observation of microwave-forced evaporative cooling of hydroxyl (OH) molecules loaded from a Stark-decelerated beam into an extremely high-gradient magnetic quadrupole trap. We demonstrate cooling by at least an order of magnitude in temperature and three orders in phase-space density, limited only by the low-temperature sensitivity of our spectroscopic thermometry technique. With evaporative cooling and sufficiently large initial populations, much colder temperatures are possible, and even a quantum-degenerate gas of this dipolar radical – or anything else it can sympathetically cool – may now be in reach.

Evaporative cooling of a thermal distribution¹⁶ is, in principle, very simple: by selectively removing particles with much greater than the average total energy per particle, the temperature decreases. In the presence of elastic collisions, the high-energy tail is repopulated and so may *repeatedly* be selectively trimmed, allowing the removal of a great deal of energy at low cost in particle number. This process may be started as soon as the thermalization rate is fast enough to be practical and continued until its cooling power is balanced by the heating rate from inelastic collisions. It generally yields temperatures deep into the quantum-degenerate regime (far below the recoil limit of optical cooling).

The key metric for evaporation is therefore the ratio of two timescales. The first is the rate of elastic collisions, which rethermalize the distribution, while the second is the rate at which particles are lost from the trap for reasons other than their being deliberately removed, e. g. the rates of inelastic scattering and background gas collisions. Both theoretical^{14,17,18} and experimental

work^{13,19,20} have seemed to show a generically poor value of this ratio across multiple molecular systems; this has led to a general belief that evaporative cooling is unfavorable in molecules¹⁵. As no trapped molecular system has achieved sufficiently rapid thermalization, there has been a lack of experiments to test this expectation.

Hydroxyl would not, at first glance, seem to be a promising candidate for evaporative cooling. Its open-shell $^2\Pi_{3/2}$ ground state and its propensity towards hydrogen bonding create a large anisotropy in the OH–OH interaction potential, which would intuitively motivate a large inelastic scattering rate. Chemical reactions are also possible, via the $\text{OH}+\text{OH}\rightarrow\text{H}_2\text{O}+\text{O}$ pathway; it is unclear whether this reaction has an activation energy barrier^{21,22}. It is thus perhaps surprising that the elastic collision rate actually exceeds the inelastic rate, allowing evaporative cooling. However, our experimental observation is unambiguous, and is further supported by quantum scattering calculations based on the long range dipole-dipole interaction between the molecules^{23,24} considering all of the fine-structure states of the rotational ground state. This analysis considers only elastic collision or inelastic relaxation to lower energy states, as the long-range interactions appear to fully dominate over short-range effects such as chemical reactions.

In its ground state, OH has a $^2\Pi_{3/2}$ electronic character, with the lowest rotational level having total non-nuclear angular momentum $J = \frac{3}{2}$. The electronic orbital angular momentum couples to the rotational angular momentum to split the two opposite-parity states within $J = \frac{3}{2}$ by a Λ -doubling of ~ 1.667 GHz; the upper parity state is labeled $|f\rangle$ and the lower $|e\rangle$. Hydroxyl is both paramagnetic, with a molecule-fixed moment of $2\mu_B$ (μ_B is the Bohr magneton), and electrically polar with a dipole moment of 1.67 Debye (5.57×10^{-30} C·m). The Zeeman spectrum of OH is shown in Fig. 1a. Our magnetic trap²⁵ is loaded with molecules in the uppermost $|f; M_J = +\frac{3}{2}\rangle$ state, where M_J is the laboratory projection of J .

The results of our scattering calculations for $|f; +\frac{3}{2}\rangle$ molecules are shown in Fig. 1b. The elastic cross section dominates the inelastic one for low energies: at a collision energy of $E_c = 50$ mK, the ratio of elastic over inelastic is $R = 5$ in a 50 mT magnetic field (B) and $R = 18$ in 150 mT, while at lower energy $E_c = 5$ mK the ratio increases to $R = 23$ and 137 respectively. Because the collisions occur in a quadrupole magnetic trap where B is inhomogeneous, the inset of Fig. 1b shows the cross sections as a function of B at $E_c = 50$ mK. This demonstrates that inelastic processes are even further suppressed at $B > 50$ mT, in agreement with previous analysis²⁴.

These scattering results can be interpreted by the emergence of an effective *repulsive* van der Waals interaction between the two molecules. In zero electric field, the effective interaction in a scattering channel m can be evaluated in second-order perturbation theory by

$$V_{\text{vdW}}(r) = \sum_n \frac{|\langle m | V_{dd}(r) | n \rangle|^2}{E_m - E_n} \sim \frac{C_6}{r^6}, \quad (1)$$

where V_{dd} is the electric dipole-dipole interaction between different scattering channels, and is non-vanishing only between molecular states of distinct parity; and E_m and E_n are the asymptotic

energies of the relevant scattering channels. For the initial molecule-molecule channel of interest $|f; +\frac{3}{2}\rangle |f; +\frac{3}{2}\rangle$, the other fine-structure channels are lower in energy ($E_n < E_m$) and repel this energy upward. Thus, the C_6 coefficient is positive, as illustrated in Fig. 1c for $B = 50$ mT, for the highest energy channel. The contribution from the next rotational state $J = \frac{5}{2}$ of the $^2\Pi_{3/2}$ manifold is too high in energy ($E_m - E_{J=5/2} \approx -100$ K) to give an appreciable attractive contribution at long-range. Hence, for low collision energies, the scattering of OH molecules is dominated by the long-range interaction rather than the short-range structure of the potential surface.

Given an effective, repulsive C_6 coefficient in the incident channel, the elastic cross section can be approximated semi-classically at energies above the threshold regime²⁶, as

$$\sigma^{\text{el}} = \frac{\pi^{11/5} (\Gamma(5/2)/\Gamma(3))^{2/5}}{\sin(\pi/5) \Gamma(2/5)} \left(\frac{\bar{C}_6}{\hbar} \right)^{2/5} \left(\frac{2E_c}{m_{\text{red}}} \right)^{-1/5} \quad (2)$$

where $m_{\text{red}} = 14497$ atomic units (a. u.) is the reduced mass of two OH molecules and $\bar{C}_6 \approx 9 \times 10^4$ a. u. is the calculated isotropic C_6 . (We contrast this \bar{C}_6 with values of $2\text{--}8 \times 10^3$ a. u. for the alkali metal atoms²⁷.) Equation (2), plotted as a red dash-dotted line on Fig. 1b, only slightly overestimates the numerical results for the elastic cross section but gives a proper trend in $E_c^{-1/5}$.

We observed inelastic scattering in the presence of a large electric field (Fig. 2b), demonstrating the presence of two-body collisions in our trapped sample. Motivated by the prediction of a favorable R , we then undertook an experiment to implement microwave-forced evaporative cooling. The $|f; +\frac{3}{2}\rangle \rightarrow |e; +\frac{3}{2}\rangle$ microwave transition has a small but nonzero differential Zeeman shift²⁸, red-shifting by 26.6 kHz/mT. In the presence of a small electric field, $|e; +\frac{3}{2}\rangle$ molecules can escape the trap through the avoided crossings labeled X_i in Fig. 1a²⁹, while inelastic losses of $|f\rangle$ molecules remain unmeasurably slow. A brief microwave pulse to selectively transfer $|f; +\frac{3}{2}\rangle$ -state molecules to $|e; +\frac{3}{2}\rangle$, followed by a longer period with an electric field present to eject $|e; +\frac{3}{2}\rangle$ molecules from the trap, is therefore a field- (position-) selective method to remove molecules from the magnetic trap (see Methods). This yields what is commonly called an RF knife (Fig. 2a). A Zeeman depletion spectrum can be acquired by using the knife to remove molecules at a set of fixed frequencies and measuring the fractional depletion ζ ; this yields a histogram of relative molecule number versus B . We fit this spectrum with a modified thermal distribution

$$\begin{aligned} \zeta(B)dB &= \zeta_0 B^2 dB \times \exp\left[-\frac{\mu B}{k_B T}\right] \times \\ &\times \begin{cases} 1, & \text{if } B > 49.6 \text{ mT} \\ \exp\left\{-\frac{\mu[(49.6 \text{ mT}) - B]}{k_B T}\right\}, & \text{otherwise} \end{cases} \end{aligned} \quad (3)$$

where ζ_0 is a fitting coefficient, $B^2 dB \propto r^2 dr$ is the volume element for a 3-D quadrupole trap, $\mu = 1.2 \mu_B$ is the magnetic moment of the $|f; +\frac{3}{2}\rangle$ state, B is the magnetic field strength implied by the microwave frequency, k_B is Boltzmann's constant, and T is the fitted temperature. The first term in the product is the simple Boltzmann expression for the molecule number as a function of

B , while the second is a correction for the fact that $|e; +\frac{3}{2}\rangle$ molecules only disappear when they go through one of the X_i crossings. Specifically, while molecules transferred at fields above 49.6 mT (the known location of $X_{-3/2}$) are always energetically able to reach one of the X_i crossings and thus disappear, of the molecules transferred at lower fields only those with enough kinetic energy to fly up the trap potential to $X_{-3/2}$ can escape the trap. This implies an additional Boltzmann factor $\exp[-\mu\Delta B/k_B T]$ in the probability of those molecules' disappearance.

With a B -selective technique for removing molecules, we easily implement forced evaporation by moving the edge of the RF knife from some large initial value of B towards zero, at a rate slow enough that the distribution remains in thermal equilibrium. Six different Zeeman spectra are shown in Fig. 3, demonstrating both forced evaporation and forced *anti*-evaporation, where for the latter the knife is held fixed at some low B_{knife} ($\mu B_{\text{knife}} < k_B T$). The trap is initially loaded with a temperature of 51 mK; left unperturbed, it free-evaporates down to 45 mK. We have forced evaporative cooling by an order of magnitude down to 5.1 mK, while forced anti-evaporation can overcome the free evaporation and increase the temperature to 54 mK. The limit of 5.1 mK is attained approximately when the RF knife edge reaches $X_{-3/2}$: while further reductions in temperature are possible, the exponential suppression of the spectroscopic signal below $X_{-3/2}$ renders our current system unable to *measure* temperatures lower than this. The plots of Fig. 3 are all normalized so that the area under the spectroscopic curve is proportional to the total $|f\rangle$ -state fluorescence signal. Thus, the increase in signal height at low B in Fig. 3c-f is direct evidence of increasing phase-space density.

The apparent *negative* signal in Fig. 3e-f can be fully fitted by assuming the presence of accumulated, trapped $|e\rangle$ -state molecules in thermal equilibrium with the visible $|f\rangle$ -state ones. Since $|e; +\frac{3}{2}\rangle$ molecules are totally trapped if they do not have enough kinetic energy to reach $X_{-3/2}$, they will *appear*, rather than disappear, during the microwave spectroscopy and contribute to the total depletion signal with a negative sign. Fitting the curves in this fashion gives even colder temperatures of 6.8 and 3.5 mK for Figs. 3e and f, respectively. As the appearance of low-energy, trapped $|e\rangle$ -state molecules would also constitute direct evidence of evaporation, we undertook a direct search and indeed detected them in laser-induced fluorescence.

We make several comments on the observed evaporation. The first is on the evaporation timescale: it is *fast*. In comparison to typical cooling rates of $d(\log T)/dt \sim 0.5 \text{ s}^{-1}$, we cool by an order of magnitude in only 70 ms, for a rate of 33 s^{-1} . This implies elastic collision rates on the order of $100\text{--}1000 \text{ s}^{-1}$, comparable to our trap frequency²⁹ of $\sim 1400 \text{ s}^{-1}$. As we are able to set a bound on the inelastic loss rate of $< 2 \text{ s}^{-1}$ (as shown in Fig. 2b), this implies a distribution-averaged $R \gtrsim 50\text{--}500$, consistent with the B -field dependence of R shown in Fig. 1b.

We quantify the behavior of the evaporation by a set of power-law scaling relations¹⁶, three of which are plotted in Fig. 4. The average energy removed per molecule, $\eta \equiv (\text{trap depth})/k_B T$, is the first metric of interest: we observe a ratio $\eta = 5.6$, as shown in Fig. 4a. (For scale, $\eta = 5\text{--}10$ is con-

sidered reasonable in atomic evaporation¹⁶.) Such a relatively low value of η is unsurprising, given both the possible low (< 1000) value of the elastic-to-inelastic ratio R and the fact that molecules are only actually lost when they cross the spatial regions corresponding to the X_i crossings. This reduces the selectivity of the RF knife, as molecules transferred to the $|e\rangle$ -state may recollide and rethermalize before they find their way to a crossing. The other metrics are the behavior of temperature and relative phase-space density (PSD) as function of remaining molecule number, shown in Fig. 4b. The efficiency of evaporation is determined by the number of molecules remaining at a given temperature and PSD, that is by $\alpha \equiv d(\log T)/d(\log N)$ and $\gamma \equiv -d(\log \text{PSD})/d(\log N)$. We measure $\alpha = 1.26$ and so using the fact that density scales as $\frac{1}{T^3}$ for our 3-D quadrupole trap we find $\gamma = 4.7$. Extrapolating this γ indicates that it would take roughly a factor of 200 reduction in number to increase PSD by 10^{10} .

We calculate both α and γ assuming that our fluorescence signal is linear with total molecule number, justified by the optical power broadening being larger than the Zeeman broadening of the trap. It is very difficult to determine the sensitivity of pulsed-laser-induced fluorescence *in situ*, so we use the observed collision rate to estimate a lower bound on the density in our trap: assuming a unitarity-limited scattering rate β_u with a maximum collisional angular momentum of $12\hbar$ (and the elastic scattering rate in Fig. 1b is only a factor of 3 below this value), an elastic collision rate of $\beta_u n_0 = 300 \text{ s}^{-1}$ implies a peak density $n_0 \approx 5 \times 10^{10} \text{ cm}^{-3}$. (Integration of a Boltzmann distribution with this peak density over the trap suggests a total number of $\sim 10^6$ molecules in the free-evaporated trap sample and an initial peak PSD of 3×10^{-10} .) This density is high enough to permit the use of absorption imaging techniques to directly visualize the trap distribution in the future. Since imaging allows direct, non-spectroscopic measurement of both density and temperature, it will enable us to quantify further reductions in temperature. With the addition of a mechanism to prevent Majorana loss¹⁶, the favorability of R down to microkelvin temperatures indicates that even Bose-Einstein condensation of OH may be feasible.

Methods Summary

Our Stark decelerator and permanent magnet trap have been described elsewhere^{25,30} and are illustrated in Fig. 2a. Briefly, OH molecules are formed by an electric discharge through a saturated mixture of water vapor in 150 kPa of krypton, supersonically expanded through a pulsed valve. The gas packet is skimmed, focused by an electrostatic hexapole, and Stark-decelerated to 34 m/s. The slowed packet is then stopped at the center of the magnetic quadrupole trap by a high-voltage field applied between the permanent magnets, and thus loaded into the magnetic trap.

Once trapped, the molecules are allowed to settle briefly (on the order of 5 ms) before evaporation begins. The evaporation sequence consists of alternating microwave (80 μs with 0 dBm at the vacuum feedthrough) and DC bias field ($\sim 650 \mu\text{s}$ at 240 V/cm) pulses: the microwave pulse selectively transfers hot molecules from the $|f\rangle$ -state to the $|e\rangle$ -state, while the DC bias destabilizes the $|e\rangle$ -state so that those molecules are lost from the trap. The microwave frequency is ramped along an exponential curve towards zero trap depth, truncated at the desired final depth.

After evaporation, the spectroscopy sequence is executed. It is similar to the evaporation, except that rather than slowly ramping a set of quasi-single-frequency pulses, each pulse is rapidly swept through the same narrow (50-500 kHz) frequency band with an additional sine-wave amplitude modulation (+10 dBm peak power at the feedthrough) so as to induce Adiabatic Rapid Passage (ARP) transference²⁹ of all the $|f\rangle$ -state molecules within the frequency band to the $|e\rangle$ -state. A DC bias field again rejects the $|e\rangle$ -state molecules from the trap. The number of ARP pulses applied is generally between 5 and 30, over a 2-10 ms spectroscopy sequence. The final molecule number is then detected by pulsed laser-induced fluorescence using the $282\text{ nm } X^2\Pi_{3/2}, v'' = 0 \rightarrow A^2\Sigma, v' = 1$ transition.

1. Anderson, M. H., Ensher, J. R., Matthews, M. R., Wieman, C. E. & Cornell, E. A. Observation of Bose-Einstein condensation in a dilute atomic vapor. *Science* **269**, 198–201 (1995).
2. Davis, K. B. *et al.* Bose-Einstein condensation in a gas of sodium atoms. *Phys. Rev. Lett.* **75**, 3969–3973 (1995).
3. DeMarco, B. & Jin, D. S. Onset of Fermi degeneracy in a trapped atomic gas. *Science* **285**, 1703–1706 (1999).
4. Bakr, W. S. *et al.* Probing the superfluid-to-Mott insulator transition at the single-atom level. *Science* **329**, 547–550 (2010).
5. Ni, K.-K. *et al.* A high phase-space-density gas of polar molecules. *Science* **322**, 231–235 (2008).
6. Pupillo, G. *et al.* Cold atoms and molecules in self-assembled dipolar lattices. *Phys. Rev. Lett.* **100**, 050402 (2008).
7. Baranov, M. A., Micheli, A., Ronen, S. & Zoller, P. Bilayer superfluidity of fermionic polar molecules: Many-body effects. *Phys. Rev. A* **83**, 043602 (2011).
8. Levinsen, J., Cooper, N. R. & Shlyapnikov, G. V. Topological $p_x + ip_y$ superfluid phase of fermionic polar molecules. *Phys. Rev. A* **84**, 013603 (2011).
9. Barnett, R., Petrov, D., Lukin, M. & Demler, E. Quantum magnetism with multicomponent dipolar molecules in an optical lattice. *Phys. Rev. Lett.* **96**, 190401 (2006).
10. Büchler, H. P. *et al.* Strongly correlated 2D quantum phases with cold polar molecules: Controlling the shape of the interaction potential. *Phys. Rev. Lett.* **98**, 060404 (2007).
11. Gorshkov, A. V. *et al.* Tunable superfluidity and quantum magnetism with ultracold polar molecules. *Phys. Rev. Lett.* **107**, 115301 (2011).
12. Ospelkaus, S. *et al.* Quantum-state controlled chemical reactions of ultracold potassium-rubidium molecules. *Science* **327**, 853–857 (2010).

13. Ni, K.-K. *et al.* Dipolar collisions of polar molecules in the quantum regime. *Nature* **464**, 1324–1328 (2010).
14. Quémener, G. & Julienne, P. S. Ultracold molecules under control! *Chemical Reviews* (in press) DOI: 10.1021/cr300092g.
15. Carr, L. D., DeMille, D., Krets, R. V. & Ye, J. Cold and ultracold molecules: science, technology and applications. *New J. Phys.* **11**, 055049 (2009).
16. Ketterle, W. & VanDruten, N. Evaporative cooling of trapped atoms. *Adv. At. Mo. Opt. Phys.* **37**, 181–236 (1996).
17. Lara, M., Bohn, J. L., Potter, D. E., Soldan, P. & Hutson, J. M. Ultracold Rb–OH collisions and prospects for sympathetic cooling. *Phys. Rev. Lett.* **97**, 183201 (2006).
18. Żuchowski, P. S. & Hutson, J. M. Low-energy collisions of NH₃ and ND₃ with ultracold Rb atoms. *Phys. Rev. A* **79**, 062708 (2009).
19. Campbell, W. *et al.* Mechanism of collisional spin relaxation in ³Σ molecules. *Phys. Rev. Lett.* **102**, 13003 (2009).
20. Parazzoli, L. P., Fitch, N. J., Żuchowski, P. S., Hutson, J. M. & Lewandowski, H. J. Large effects of electric fields on atom-molecule collisions at millikelvin temperatures. *Phys. Rev. Lett.* **106**, 193201 (2011).
21. Atkinson, R. *et al.* Evaluated kinetic and photochemical data for atmospheric chemistry: Volume I - gas phase reactions of O_x, HO_x, NO_x and SO_x species. *Atmos. Chem. Phys.* **4**, 1461–1738 (2004).
22. Bahng, M.-K. & Macdonald, R. G. Determination of the rate constant for the OH(X²Π) + OH(X²Π) → O(³P) + H₂O reaction over the temperature range 293–373 K. *J. Phys. Chem. A* **111**, 3850–3861 (2007).
23. Avdeenkov, A. V. & Bohn, J. L. Collisional dynamics of ultracold OH molecules in an electrostatic field. *Phys. Rev. A* **66**, 052718 (2002).
24. Ticknor, C. & Bohn, J. L. Influence of magnetic fields on cold collisions of polar molecules. *Phys. Rev. A* **71**, 022709 (2005).
25. Sawyer, B. C., Stuhl, B. K., Wang, D., Yeo, M. & Ye, J. Molecular beam collisions with a magnetically trapped target. *Phys. Rev. Lett.* **101**, 203203 (2008).
26. Child, M. S. *Molecular collision theory* (Dover Publications, 1996).
27. Derevianko, A., Johnson, W. R., Safronova, M. S. & Babb, J. F. High-precision calculations of dispersion coefficients, static dipole polarizabilities, and atom-wall interaction constants for alkali-metal atoms. *Phys. Rev. Lett.* **82**, 3589–3592 (1999).

28. Lev, B. L. *et al.* OH hyperfine ground state: From precision measurement to molecular qubits. *Phys. Rev. A* **74**, 061402 (2006).
29. Stuhl, B. K., Yeo, M., Sawyer, B. C., Hummon, M. T. & Ye, J. Microwave state transfer and adiabatic dynamics of magnetically trapped polar molecules. *Phys. Rev. A* **85**, 033427 (2012).
30. Bochinski, J. R., Hudson, E. R., Lewandowski, H. J., Meijer, G. & Ye, J. Phase space manipulation of cold free radical OH molecules. *Phys. Rev. Lett.* **91**, 243001 (2003).

Acknowledgments We thank E. Cornell for useful discussions and B. Baxley for artistic contributions. We acknowledge funding from the NSF Physics Frontier Center, DOE, AFOSR (MURI), and NIST.

Contributions B.K.S., M.T.H., M.Y., and J.Y. designed and participated in the experiment, discussed and interpreted the results. B.K.S. ran the day-to-day experiment and collected all the data. G.Q. and J.L.B. constructed the theory. B.K.S. and J.Y. first outlined the manuscript, and B.K.S. and G.Q. wrote the first draft. All authors discussed the results and contributed to the preparation of the manuscript.

Competing Interests The authors declare that they have no competing financial interests.

Correspondence Correspondence should be addressed to Jun Ye (email: ye@jila.colorado.edu).

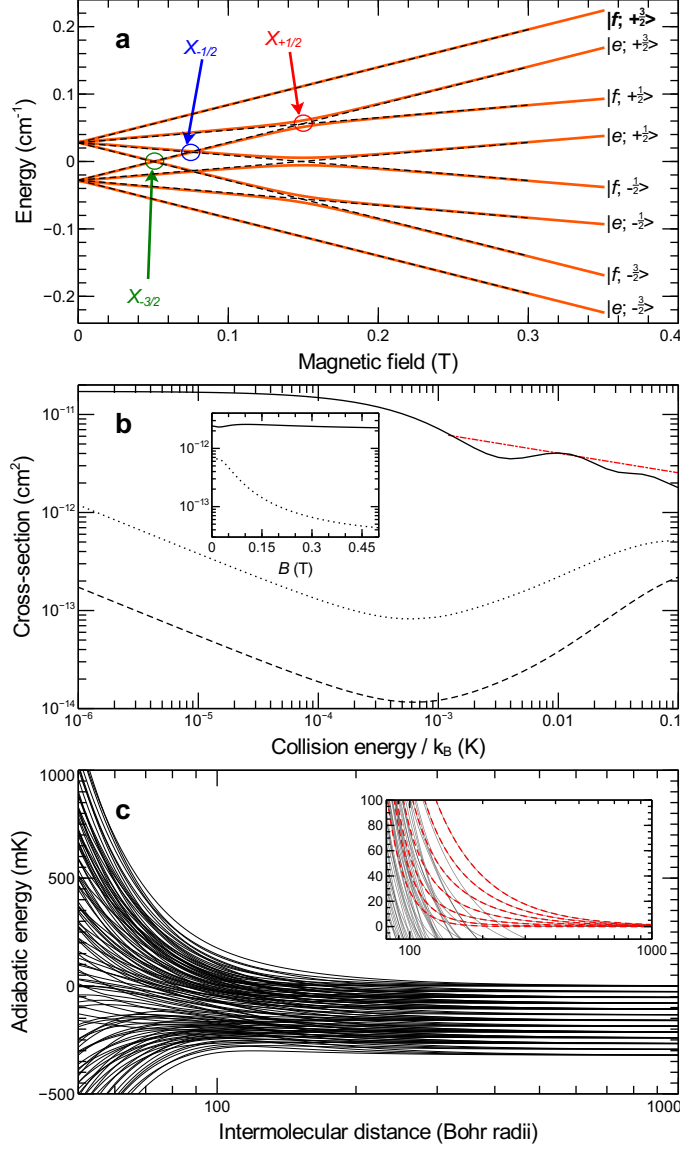


Figure 1: **Ground-state structure and scattering theory of OH.** **a**, The ground-state Λ -doublet and Zeeman structure of OH. Dashed black lines are energy levels in the absence of any electric field. In the presence of an electric field, the level crossings become avoided (solid orange lines). X_i label the crossings of the $|e; +\frac{3}{2}\rangle$ state with the $|f; M_J = i\rangle$ states; these crossings allow $|e; +\frac{3}{2}\rangle$ molecules to escape the trap in the presence of an electric field. Molecules are loaded into the magnetic trap in the bolded $|f; +\frac{3}{2}\rangle$ state. **b**, Cross sections as a function of collision energy: elastic cross section in a 50 mT magnetic field (solid), inelastic in 50 mT (dotted), and inelastic in 150 mT (dashed). The red dash-dotted line is a semi-classical expression given by Eq. (2). Inset: elastic (solid) and inelastic (dotted) cross sections as a function of magnetic field at $E_c = 50$ mK. **c**, Adiabatic energies as a function of the inter-molecular distance at $B = 50$ mT. The inset zooms in on the repulsive van der Waals interaction for the case of two colliding $|f; +\frac{3}{2}\rangle$ molecules.

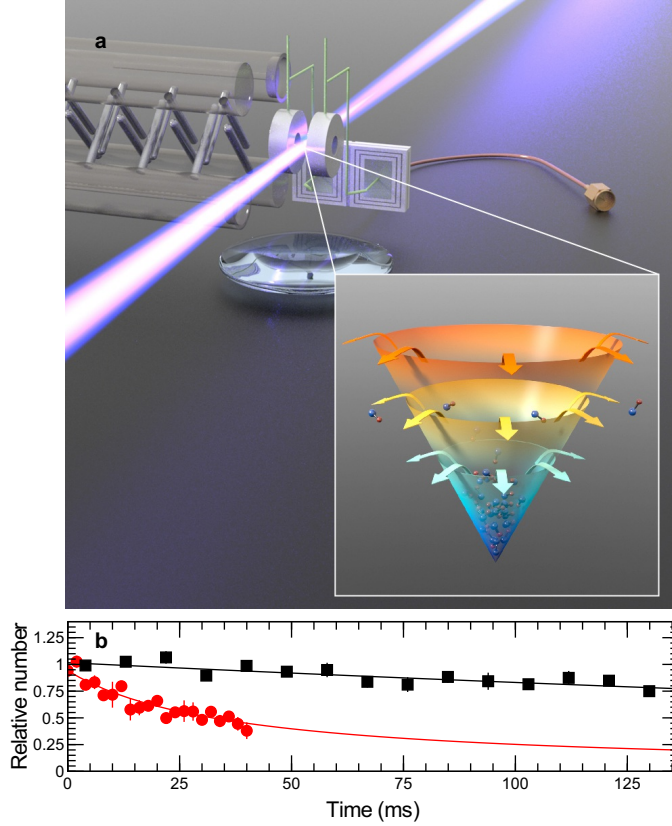


Figure 2: Trap system and inelastic collisions. **a**, Schematic of the Stark decelerator³⁰ (left) and magnetic trap (center rings) system. The DC-blocking capacitor (rear) decouples the high voltage used for trap loading from the microwave system used for spectroscopy and evaporation, while the laser and lens provide fluorescence detection of the trapped molecules. Inset: an artist's impression of evaporative cooling. As the trap depth is successively lowered by the RF knife, the hottest molecules escape and the remainder rethermalize to a colder temperature. **b**, Time-of-flight trace of electric field-induced collisions at 45 mK. Black squares, consistent with pure one-body loss, are with no applied electric field; red circles are well-fit by pure two-body inelastic loss induced by a large applied electric field of 3040 V/cm. (The field used in the RF knife is only 240 V/cm, for comparison.) Error bars are one standard error.

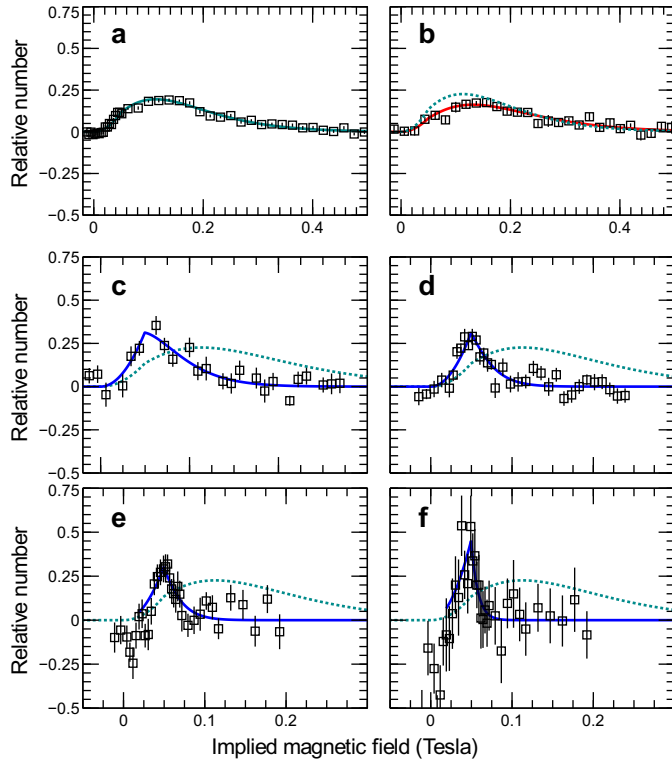


Figure 3: **Microwave spectra illustrating six different final temperatures.** Black squares are data (error bars are 1 standard error), and solid lines are fits to the sensitivity-corrected Boltzmann form of Eq. (3): **a** the unperturbed 45 mK distribution, **b** *anti*-evaporation to 54 mK, **c-f** forward evaporation to **c** 18 mK, **d** 12 mK, **e** 9.8 mK, and **f** 5.1 mK. Dotted lines reproduce the fit from **a**, shown for comparison. Note that the x-axis scale differs between **a-b** and **c-f**; all curves have been shifted vertically to have a zero baseline.

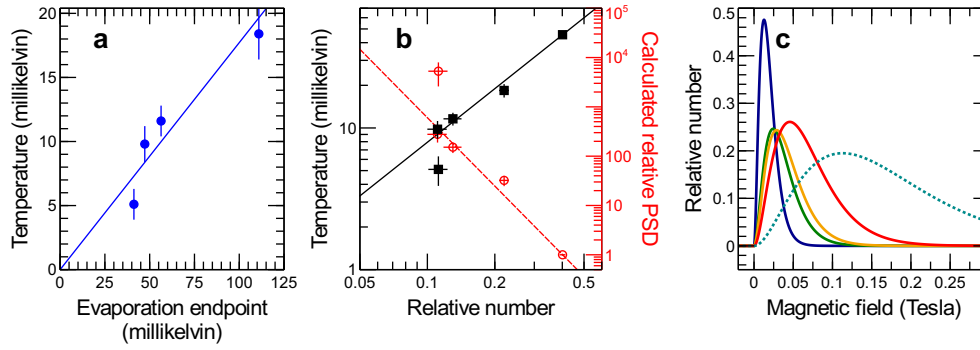


Figure 4: **Scaling relations observed in the evaporative cooling of OH.** **a**, Final observed temperature versus effective trap depth at evaporation ramp end. **b**, Final temperature (solid black, left axis) and calculated relative phase-space density (dashed red, right axis) versus remaining relative molecule number. Error bars are 1 standard error; phase space density is calculated assuming a 3-D quadrupole trap geometry. **c**, Molecular Boltzmann distributions implied by the fit curves of Fig. 3a and c-f (right to left). Distributions are normalized so that the area under each curve is proportional to the total $|f\rangle$ -state fluorescence observed at that temperature.